Energy-absorption capacity of additively manufactured AlSi10Mg cellular structures subjected to a blast-induced dynamic compression–experimental and numerical study

Piotr Pawlowski [a] , Magda Stanczak [b,c] , Paula Broniszewska-Wojdat [a] , Ludovic Blanc [b] , Teresa Fras [b,*] , Alexis Rusinek [c]

[a] *Institute of Fundamental Technological Research Polish Academy of Sciences, Warsaw, Poland*
[b] *French-German Research Institute of Saint-Louis (ISL), Saint-Louis, France*
[c] *University of Lorraine, CNRS UMR 7239, Arts et Métiers Sciences et Technologie, LEM3, Metz, France*

ARTICLE INFO

ABSTRACT

The study investigates the role of the topology of the additively manufactured AlSi10Mg cellular structures in the example of 3D and 2D designs: honeycomb, auxetic, lattice and foam. The samples were subjected to quasistatic and blast-induced dynamic compression. As a result, a relation between the structural geometry and the deformation mode of the compressed structures has been developed, demonstrating its influence on the energy absorption characteristics. The deformation and fracture mechanisms were examined in detail using the finite element simulations in the LS-DYNA code based on the material characterisation over a broad range of strain rates and temperatures. The outcomes show an agreement between the experimental data and the computations. The obtained results prove that by selecting the appropriate topological features, the deformation of compressed structures can be enhanced to improve their energy-absorption capacity.

1. Introduction

Under compressive loading and an impulse impact in particular, metallic cellular structures can undergo significant deformation and further controlled fracture of subsequent cells. A failure of one cell is followed by a neighbouring one, causing the arrays of nearby cells to collapse progressively along the introduced failure pattern. Due to this progressive failure, the cellular structures absorb more impact energy than the bulk material with a comparable relative density. A controlled failure mechanism may ensure energy is absorbed steadily and predictably over a relatively long displacement. Boundary conditions, relative density, volume percentage, and the geometry of the cellular structures (strut length, thickness, angles between them, and the arrangement of the cells) all affect the progressive collapse mechanism. Different progressive failure mechanisms for four re-entrant-star-shaped structures produced from PLA using stereolithography are discussed, presenting clearly the influence of the geometry on the mechanism of progressive collapse [1]. Boundary conditions and elastic and plastic wave propagation influence the progressive collapse mechanism within cellular structures. Furthermore, the sensitivity to strain rate is another

key factor that affects the collapse behaviour. These parameters collectively affect a given cellular structure's buckling and collapse characteristics [2].

Periodic cellular structures offer more design freedom and customisable mechanical properties than foams with random or stochastic geometries. The energy absorption characteristics may be improved by adjusting parameters like cell size, shape, and material. Much research has been conducted on the performance of periodic cellular structures due to the numerous industrial uses in aerospace, automotive and defence engineering. At the dawn of their wide industrial applications, the research focused on the fundamental mechanical characteristics of thin-walled aluminium honeycombs, e.g. Gibson and Evans [3,4]. Further, Abramowicz and Jones [5], McFarland and Wierzbicki [6–9] examined elementary cellular structures under crashing loadings. Through empirical and analytical approaches, they described the kinematics of the plastic collapse mechanisms. Numerous studies have also demonstrated that the periodic cellular structures possess superior blast resistance compared to monolithic plates of equal mass, e.g. [10–12].

Honeycombs and auxetics are among the most widely used cellular structures comprising 2D unit cells. These structures are applied where it

---

* Corresponding author.
  E-mail address: teresa.fras@isl.eu (T. Fras).

is necessary to convert compressive planer stress into compressive longitudinal stress [13,14]. Thin-walled aluminium honeycombs are applied to minimise rapid crashing load because of their high strength-to-weight ratio and cost-effective and efficient production process. Nonetheless, there are notable distinctions between honeycombs' in- and out-of-plane characteristics, such as strength or stiffness. The 2D cellular structures might not be appropriate when the loading direction is not axial because of their strong orthotropic behaviour [15]. However, 3D cellular structures are free of this flaw. Popular representations of a 3D unit cell group include lattices and foams. Unlike the 2D cellular structures, their response to loads is not restricted to a single direction, thus offering higher operational flexibility. While it is generally observed that lattices and foams often exhibit higher strength than certain auxetic designs, this relationship strongly depends on the relative density of the materials being compared. Auxetic structures with higher relative densities demonstrate superior strength in specific scenarios. More information about the cellular structures may be found in [16–19].

More complex periodic cellular structures may necessitate an intricate production procedure. Additive manufacturing offers several advantages in producing enhanced and optimised geometries. A great flexibility of innovative designs is obtained by a particular technique in which a laser melts one powder layer and fuses it with the previous one. Due to this layer-over-layer material depositing process, components with a nontrivial geometry may be fabricated. In additive manufacturing, material selection, process parameters, and post-process are important steps that aid in achieving the intended material and geometrical characteristics of the final product. Various materials may be employed in metal additive manufacturing, including steel, aluminium and titanium alloys. Due to its good mechanical qualities and low thermal expansion, the AlSi10Mg alloy is an especially favoured Al-based alloy used in additive manufacturing for complex lightweight designs.

Studies on additive manufacturing techniques are becoming increasingly common due to the wide industrial popularisation of structures obtained through this technique. Many investigations focus on AM technology and possible ways of its improvements, e.g. [20,21]. Investigation of metal powders in application to the AM techniques is also well represented, e.g. [22,23]. Gite et al. [24] reviewed selective laser melting printing parameters, microstructure, heat treatment, and mechanical properties of additively manufactured AlSi10Mg aluminium alloy. Another popular research area is an analysis of material properties and mechanical characteristics of AM materials in 'as-printed' or processed conditions. The mechanical behaviour of AlSi10Mg alloy produced by Laser Powder Bed Fusion was investigated utilising a combined experimental and modelling approach in the study of Logakannan et al. [25]. The effects of heat treatment on the AM-fabricated AlSi10Mg samples were analysed in detail. The hardness and tensile testing proved that the heat-treated samples were more ductile than the as-printed ones. The study aimed to determine the fracture locus of the additively manufactured AlSi10Mg material. The performed tests included uniaxial compression, shear, and uniaxial tensile tests on dog-bone type and notched samples. Numerical simulations were performed to confirm the triaxiality values. Failure strain versus triaxiality curves for the samples printed along three orientations revealed negligible dependency of the material fracture loci on the building orientation. The study emphasises the importance of triaxiality-based failure criteria in predicting the failure of additively manufactured structures.

Understanding the mechanical response of the AlSi10Mg additively manufactured structures under various strain rates is the objective of the study of Ghisi et al. [26], who analysed data from as-built samples fabricated in three orientations and subjected to tensile loading in quasistatic and dynamic regimes. The influence of the building direction was investigated and correlated to the resultant microstructure. The study reports on strain rate sensitivity and the fractography of tested samples. The fractography analysis elucidated the effects of different deformation rates on failure modes and the accompanying microstructural changes. Despite presenting low strain rate sensitivity and no evidence of large strain hardening, the strain rate influenced the fracture response and elongation to failure. Microstructural changes were captured on the fracture surfaces for higher strain rates, suggesting localised in-situ thermal changes due to the adiabatic effects of high-velocity loadings.

Cellular structures have the potential for efficient protection against dynamic loadings, especially during high-strain rate scenarios such as a blast. Additive manufacturing enables the design of complex geometries to optimise structural architecture and, thus, increase blast resistance. Wei et al. [27] combined experimental and numerical approaches to analyse the response of additive-manufactured sandwich panels subjected to a proximity air blast loading. Auxetic honeycombs were fabricated from the Ti–6Al–4V alloy via Selective Laser Melting. Uniaxial tension tests and metallurgical investigations were conducted to reveal the mechanical response and microstructure of the AM alloy. Blast tests were carried out to characterise the deformation and failure of the blast-loaded Ti–6Al–4V sandwich panel. Computational models validated with the experiment provided insights into the tested structures' dynamic deflection, crack propagation, and pressure wave evolution. This study demonstrated the feasibility of using AM sandwich panels with designed auxetic honeycomb cores as modern protective structures for enhanced blast resistance.

Small-scale explosive loading of sandwich panels with low relative density pyramidal lattice cores has been used to study the large-scale bending and fracture response of a model sandwich panel system in which the core has little stretch resistance in the work of [28]. The experiments of [29] focus on the out-of-plane compression of stainless steel cellular materials fabricated using selective laser melting (SLM) and make two specific contributions. They demonstrated how the AM process influences the characteristics of these cellular materials across a range of length scales and, crucially, how this influences dynamic deformation. It was also shown how an AM route can add geometric complexity to the cell structure, creating a versatile basis for future geometry optimisation. Starting with an AM square honeycomb, the porosity of the walls was changed by replacing them with a lattice truss while maintaining the same relative density. This geometry hybridisation is an approach uniquely suited to this manufacturing route. It is found that the hybrid lattice-walled honeycomb geometry significantly outperforms previously reported AM lattices in terms of specific strength, specific energy absorption, and energy absorption efficiency. It is also found that the hybrid geometry outperforms the benchmark metallic square honeycomb in terms of energy absorption efficiency in the intermediate impact velocity regime (i.e. between quasistatic loading and loading rates at which wave propagation effects begin to become pronounced), a regime in which dynamic buckling effects dominate the collapse. Ramos et al. [30] aimed to design blast-resistant lattice structures that improve protection efficiency under high-strain rate loadings. Hybrid-layered Triply Periodic Minimal Surfaces (TPMS) lattice structures were designed using a Design of Experiments (DoE) approach and manufactured additively from the SS316L steel. The Blast Hopkinson Pressure Bars setup was used to compare the influence of different lattice topologies and relative densities on energy absorption when specimens were subjected to compressive blast loading. Due to high-speed imaging, transient deformation and the load transferred through the specimens were measured. The experimental results indicate that the setup used can appropriately measure the energy absorption of compressive structures subjected to an impulsive loading induced by a blast wave resulting from a detonation of an explosive charge. Additionally, the results demonstrate that the topology and relative density changes affect energy absorption mechanisms.

The following publications [31–36] were prepared in the same working circle and preceded the current study. The first study [31] comprehensively explains the experimental methods used in the EDST technique. Its main topic is the experimental and analytical analysis of
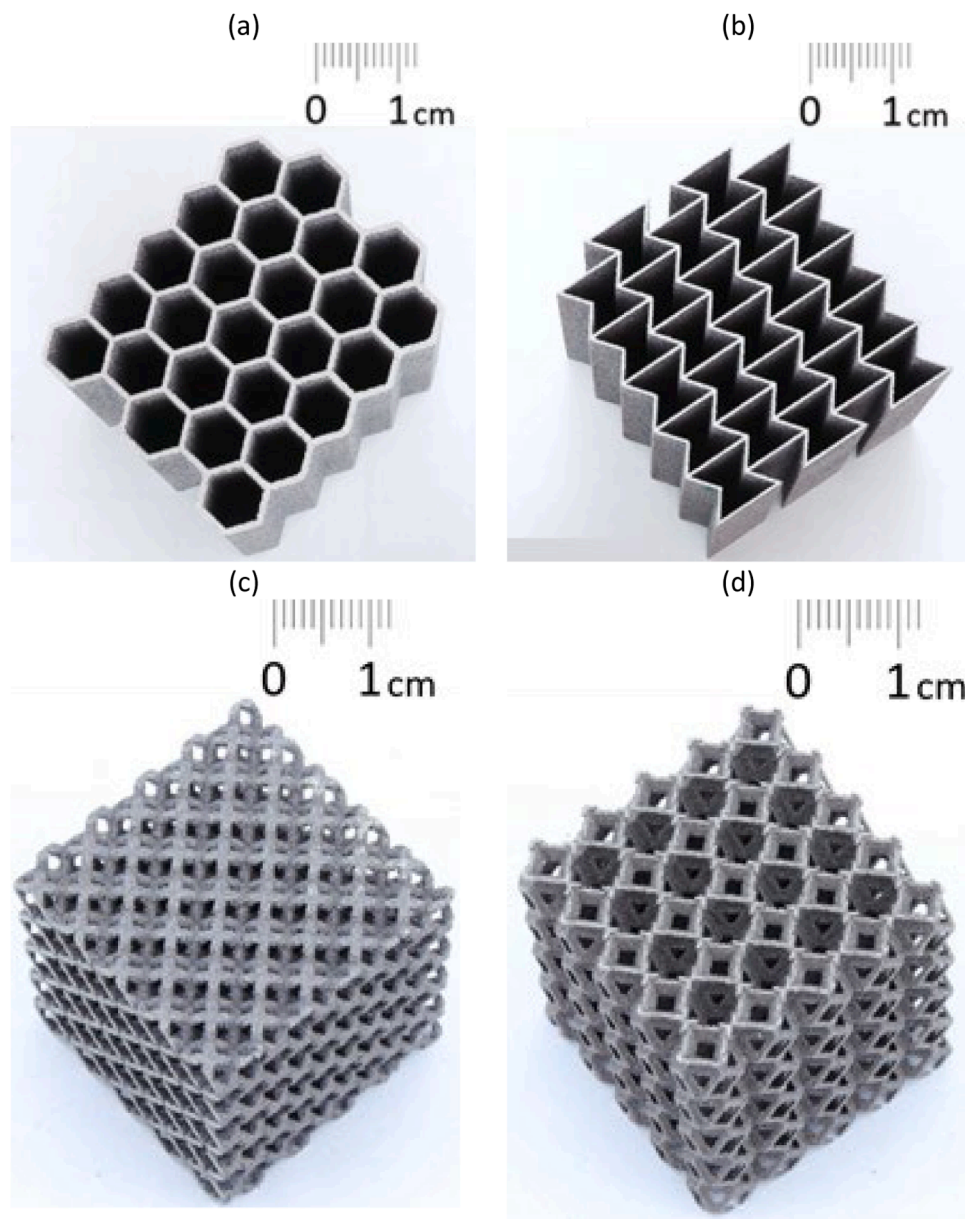
Fig. 1. Manufactured AlSi10Mg structures: (a) honeycomb, (b) auxetic, (c) lattice, (d) foam.

momentum transmission during the crushing of the core, considering the fluid-structure interaction effect, the core's mechanical behaviour, and the pneumatic effects generated by the trapped air in its cells. The work demonstrates that the mechanical behaviour of the core often counterbalances the beneficial effects of fluid-structure interactions, and analytical models from the literature suffice to describe the magnitude of the uniaxial crushing process. Based on the experimental results, Kambouchev's model was validated to describe FSI effects and project a free-standing plate under a blast load. The study [32] concerns a microstructural analysis that compares the heat-treated and 'as-received' structures of additively manufactured AlSi10Mg. The paper discusses the material behaviour of the AM-aluminum alloy based on the results of quasistatic and dynamic compression experiments conducted across a wide range of strain rates and temperatures. The current manuscript utilises the results of that study to provide the reader with an insight into the material's performance and properties. Primarily, we used these data for material modelling, which is essential for the numerical simulation of the conducted blast tests. The studies [33,34] focus on the blast-induced compression of the conventional thin-walled

aluminium honeycomb, providing an analysis of the experimental technique of the Explosively Driven Shock Tube and detailed numerical aspects of the modelling of blast-induced dynamic compression. Finally, the studies [35,36] focus on the additively manufactured AlSi10Mg structures, offering subsequent data on the blast test and the behaviour of the cellular structures under such loading.

The current study investigates energy-absorption properties, deformation and failure modes of additively manufactured 3D and 2D cellular structures, i.e., foam, lattice, auxetic, and honeycomb. The material characterisation was obtained based on strain rate and temperature-dependent testing. The Explosively-Driven Shock Tube (EDST) setup compresses the manufactured cellular structures in dynamic conditions. Quasistatic compression tests were also performed and analysed for comparison. The tested samples were in as-printed conditions. The scaling effect of the relative density on the mechanical characteristics and the specific energy absorption (SEA) of the tested structures was evaluated. A numerical simulation was prepared to analyse the deformation modes and collapse patterns of the AM structures crushed in the blast experiment. The proposed approach validated the structures'

Table 1
Some characteristics of the tested AM AlSi10Mg structures.

	Lattice	Foam	Honeycomb	Auxetic
Dimensions [mm] $a \times b \times$ h	29.89 × 29.87 × 29.96	30.22 × 30.21 × 30.8	27.14 × 32.34 × 29.92	29.91 × 29.43 × 32.18
Mass [g]	17.4	14.3	11.9	10.8
Relative density [-]	0.21	0.19	0.17	0.15

Table 2
Basic parameters used for manufacturing the tested structures by the DMLS method of the EOSINT M280 printer.

Parameter of printing process	Value
Power of the laser source	370 W
Scan velocity	1300 mms^{-1}
Hatch distance of the laser scan tracks	190 μm
Thickness of the powder layers to be scanned	30 μm
Energy density	50 Jmm^{-3}

Table 3
Chemical composition of the AlSi10Mg aluminum powder (a) and (b) the printed, not-processed material following the producer [21].

		Alloying elements [wt%]				
(a)	AlSi10Mg powder	Al Bal.	Si 9 −11	Mg 0.2–0.45	Fe ≤0.55	Mn ≤0.45
(b)	**AlSi10Mg 'as-printed'**	ν	$\rho_m \left[\frac{g}{cm^3}\right]$	E [GPa]	$\sigma_{YS}[MPa]$	$\sigma_{UTS}[MPa]$
		0.33	2.67	70	(XY) 270 ±10 (Z) 240 ±10	(XY) 460 ±20 (Z) 460 ±20

performance and may indicate their possible improvements to attenuate blast loadings.

2. Material and specimens

Four types of AlSi10Mg aluminium cell structures have been prepared for the experimental investigation, as presented in Fig. 1. The auxetic and honeycomb represent structures comprising unit cells that fit into two dimensions. In contrast, a foam and a lattice structure represent a 3D geometry of the unit cell. The 3D and 2D structures are based on cubes with edges measuring 30 mm and have five unit cells along the length direction. The measured thickness of the walls varies between 0.38 mm and 0.56 mm. With the generally same volume, the structures have different masses, which is summarised in Table 1. Therefore, they are characterised by slightly different but comparable relative densities. The honeycomb has a relative density of 0.17 and an auxetic of 0.15, whereas for the foam and lattice, it is 0.19 and 0.21 adequately [36].

The specimens were produced from the AlSi10Mg aluminium powder using the EOSINT M280 printer and DMLS (Direct Metal Laser Sintering) technique. The DMLS system is equipped with a fibre laser with a wavelength of 1060–1100 nm and a maximal power of 400 W. The precision of the laser beam in the building area, varying between 100–500 μm, ensures the depth of the beam melting around three layers of powder (20–60 μm). The exposure speed of the scanner can be up to 7000 mms^{-1}. The linear drive moves the recoated arm horizontally with a 40–500 mms^{-1} travel speed. After the sintering process of the first layer, the build platform is lowered by one layer height, giving space for the next powder layer (20–100 μm). The laser beam melts a powder layer, and the print operation can be repeated. The excess powder goes to the collector platform, which can be reused after sifting. Table 2 displays the used printing settings. Table 3 presents the AlSi10Mg powder chemical composition. The powder comprises particles of a diameter ranging from 10 to 45 μm. Following the producer datasheet [37], some of the final printed parts' properties in the as-fabricated state are also collected in the table. The resulting density of the manufactured bulk material is 2.67 gcm^{-3}. A large thermal gradient, rapid melting, and solidification characteristics for additive manufacturing allow for

(a)

(b)
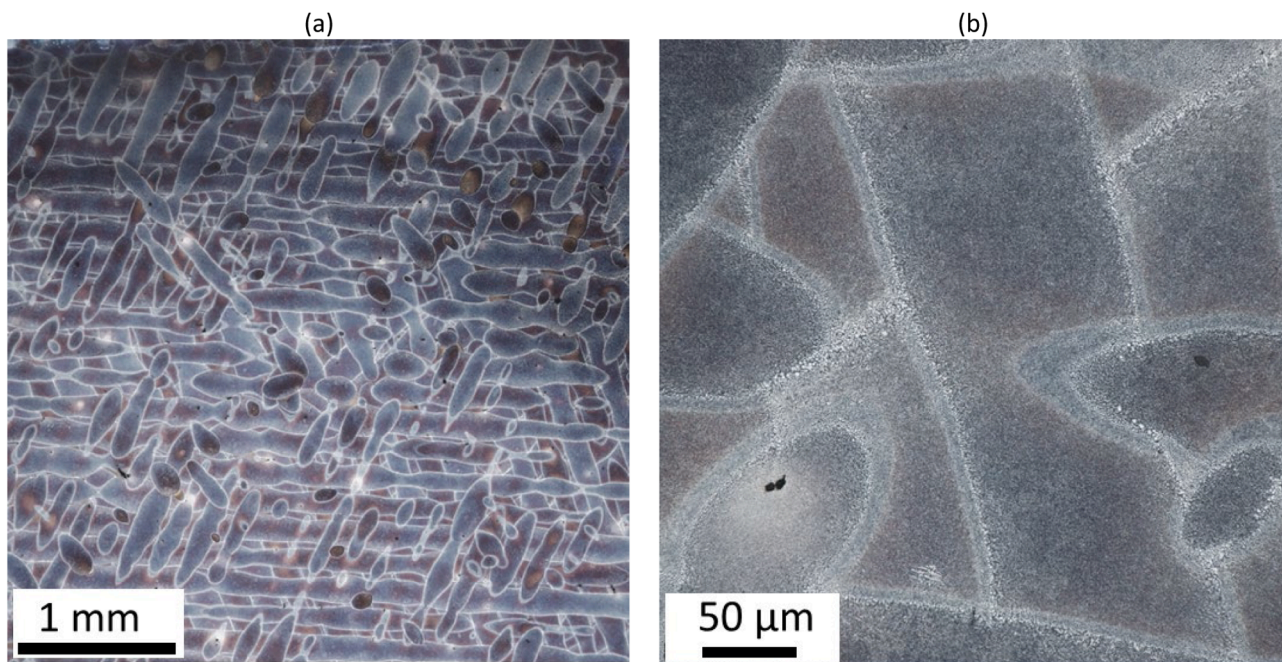
Fig. 2. Optical microscopy images of the microstructure of the manufactured AlSi10MG alloy presenting a cross-section perpendicular to the building direction (a) with a close-up (b).
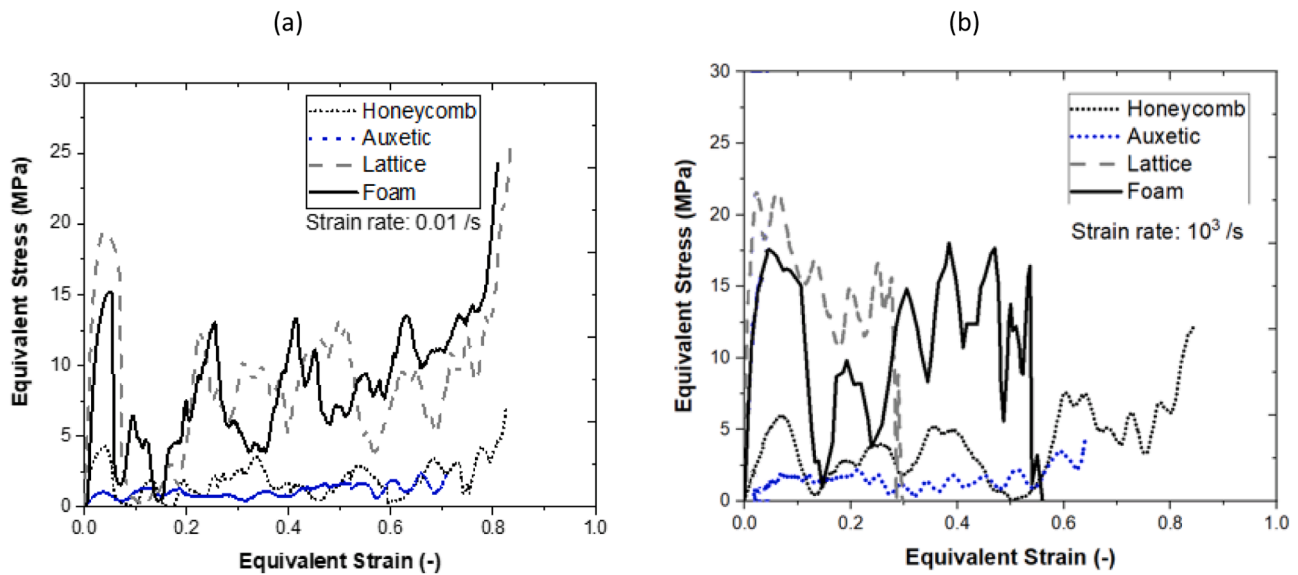
Fig. 3. Equivalent stress vs equivalent strain for the quasi-statically (a) and dynamically (b) compressed AlSi10Mg structures.

obtaining ultra-fine grain size with visible diversion into melt pools, Fig. 2. The grains in the interior of melt pools are columnar and oriented towards the energy source. In contrast, grains at the border are finer and equiaxial. A whole microstructure is dominated by the eutectic Al-Si phase, which is the reason for the higher durability of the additively manufactured AlSi10Mg alloy compared to the cast one.

3. Experimental investigation

Four representative types of printed structures were tested under quasistatic and blast-induced dynamic compression (Fig. 4). The tests allowed us to observe the behaviour of the AM structures with different geometries based on the recorded experimental evidence and compare the influence of the structural properties on the energy-absorption properties.

3.1. Quasistatic compression test

A hydraulic universal testing machine, an Instron 5982 equipped with a 100 kN load cell, was used to conduct quasistatic compression tests of the four additively manufactured structures. For the tested 30 mm high structures, a constant 0.01 s^{-1} strain rate of deformation was realised at a loading velocity of 18 mms^{-1} of the UTM's movable grip. The compressed sample was placed between two high-hardness steel plates without lubricant for testing. The UTM's data acquisition system registered the force and the displacement, which were recalculated into the equivalent stress-strain presented in Fig. 2(a). A camera followed the subsequent tests, providing snapshots of the deformation process, Fig. 4.

3.2. EDST blast test

The dynamic response of the tested AM structures was investigated using an Explosive-Driven Shock Tube (EDST) test stand, presented in Fig. 5 [30,33]. Limiting the spherical spreading of the blast wave and forcing its propagation inside the tube of 80 × 80 × 1750 mm^3 tube guarantees the travel of a planar front. Detonation of explosive charges of reduced masses (30 g of C4 in the current study) generated a planar blast wave with high intensity, due to which samples with larger representative elementary volumes were tested under blast-induced compression. Fig. 5(c) presents the time evolution of the pressure generated by detonations of charges with three different masses. In the test, in which 30 g of C4 was detonated, and no absorptive structure was

inserted into the test setup, the velocity of an eight mm-thick S235 plate was calculated as 25 ± 2 m/s. The pressure generated by the explosion is converted into the planar displacement of the front plate, which compresses the crushable core, delaying the transmission of the load to the target. The reflected blast load parameters are measured at the end of the tube with a Kulite HKS-375 pressure transducer installed on a rigid plate, closing the tube. These data provide the reference force and impulse loads transmitted to a hypothetical rigid layered assembly. For a detailed discussion, see [31], in which the momentum transmission during the crushing of the core has been experimentally investigated, taking into account the fluid-structure interaction effects.

For testing, each sample was set between two S235 steel plates of 100 × 100 mm^2, Fig. 5(a–b). The front surface of the tested structures was in contact with an eight mm-thick steel plate with a mass of 655 g, whereas its rear surface contacted an 11 mm-thick steel plate mounted in the concrete wall of the bunker. In the EDST setup, the pressure generated by the explosion is converted into the axial displacement of the front plate, which compresses the structure, dissipating the generated energy through the structure's plastic deformation and fracture [30,31,36]. To register the transmitted force over time, the piezoelectric force sensor PCE206C (13.5 mV/kN, with a measurement range of 355.86 kN) was placed behind the bottom surface of the sample. A high-speed camera, the Phantom V311, tracked the moving plate's displacement and registered the samples' deformation. The representative time-frames are given in Fig. 6. The camera has a total recording time of 2 s, delivering a speed frame rate of 31 fps. The f85/1.4 lens with an exposure time lower than eight μs, the 1280 × 800 CMOS sensor ensures an adequate time discretisation to measure the displacement of the front plate through image analysis.

The EDST allows investigation of the structure's global deformation; each characteristic is assumed to represent an equivalent homogenised material. Consequently, while the material strain rate cannot always be efficiently measured using this setup, it is possible to assume the structure as a homogeneous material, which would then be submitted to a strain rate up to 1 × 10^3 s^{-1}. Fig. 3 shows the resulting stress-strain responses of the tested additively manufactured cellular structures. Fig. 7 compares the calculated absorbed energy. More information on this experimental technique may be found in [30,31,36].

4. Results and discussion

When looking at the graphs in Fig. 3, it may be noticed that the

Table 4

Some characteristics of the quasi-statically (a) and dynamically (b) compressed AM structures.

		Lattice	Foam	Honeycomb	Auxetic
(a)	Peak stress [MPa]	19.57	15.21	4.29	1.06
	Mean stress [MPa]	8.28	7.97	1.51	1.12
	Densification strain [-]	0.78	0.76	0.82	0.68
(b)	Peak stress [MPa]	21.56	17.43	6.01	1.75
	Mean stress [MPa]	14.18	10.49	3.52	1.44
	Densification strain [-]	0.31	0.52	0.80	0.58

registered compressive curves of four AM structures in the quasistatic and dynamic regimes show three phases: peak, plateau, and densification, characteristic for the compression of conventional cellular structures (like a thin-walled aluminium honeycomb, for instance [2,3,36]). The values of the peak and mean stresses and the densification strains read for the quasistatic and dynamic compression of the structures are given in Table 4. The theoretical basis of the calculations may be found, for example, in [2,3].

For the tested additively manufactured structures, the first phase is a linear elastic deformation that ends in a clear peak. Occurred due to compression, a plastic collapse of specific cell region leads to a sudden increase of stresses, and thus a formation of the first registered peak. Regardless of the deformation rate, the highest peak stress characterises
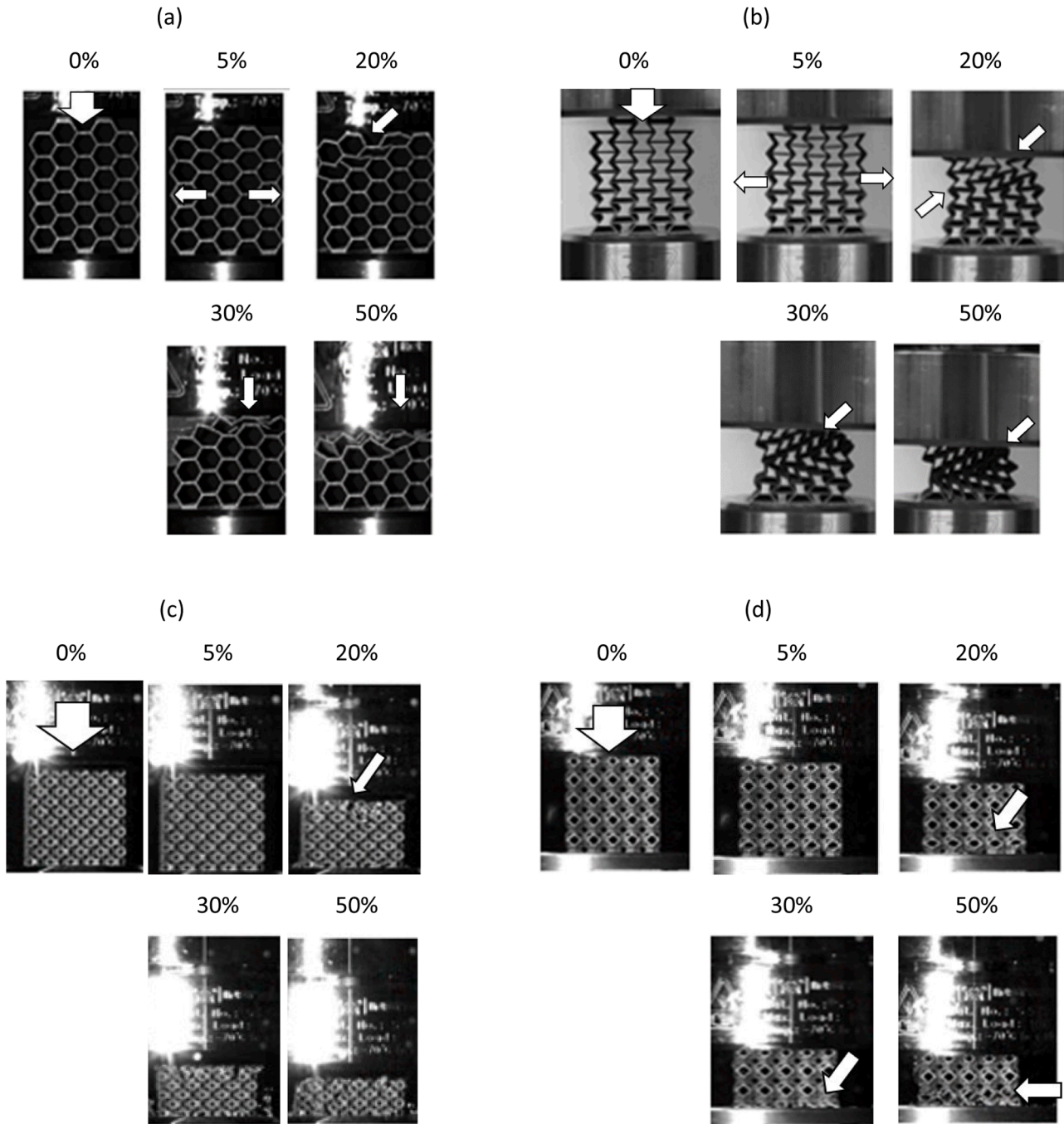
Fig. 4. The subsequent phases of the quasi-static compression of (a) honeycomb, (b) auxetic, (c) lattice and (d) foam structures presented in the progress of deformation.

the lattice (about 20 MPa and 22 MPa for the quasistatic and dynamic compression), which is, among the tested samples, the heaviest structure with the highest relative density (0.21). Furthermore, the foams' peak stress is 15 MPa (at quasistatic rates) and 17 MPa (in dynamic compression). The honeycomb and the auxetic structures reached their peak stresses of 4 MPa and 1 MPa due to the quasistatic compression and 6 MPa and 2 MPa in the dynamic compression. These two 2D-type structures have the lowest relative density of 0.17 and 0.15.

The notable oscillations, especially strongly visualised in the dynamic blast-induced compression, feature all structures' responses in the equivalent stress-strain curves. The ductile-brittle nature of the failure modes occurs through breaking the ligaments bonding the structures' cells. The structures are fully distorted and reach the densification stage when the struts start coming more and more into contact with each other because of a lack of space, restraining plastic deformation – as evidenced by sharp curves' rises and drops. This stage may be associated with the yielding of the material and the further damaging processes, including bending or collapsing.

The presence of multiple peaks prior to the densification phase, as observed in Fig. 12(c), arises from a combination of factors. These include inertia effects and strain rate sensitivity, which become pronounced under dynamic loading conditions. The finite ratio of unit cell size to the total block dimensions also contributes to localised stress variations and wave interactions within the structure. Regarding the sudden increase in stresses attributed to the plastic collapse of specific cell regions, this may not directly correspond to a visible increase in the slope of the stress-strain curve in the figures. This discrepancy is due to the redistribution of stresses and energy dissipation mechanisms, which do not always result in a monotonic increase in the curve's slope. Each significant deformation is reflected on the stress-strain curve. Oscillations registered in the graphs may be affected by several factors, not only originate from the structure deformation. Its influence may also have a measurement approach (in which the used load sensor might have led to oscillations of the measurement plate at a specific frequency, about 11 kHz), the inertia effect or the ratio of unit cell size to total block. A numerical simulation may be beneficial for analysing the structure responses since it is free from certain in-field effects of the experimental technique. The authors of [38,39] observed that the three-row gradient auxetic honeycomb made with AM Titanium alloys had peaks observed during the compression process, which can be attributed to the deformation and collapse of the three-layer structures. A significant stress drop makes each failure visible because tested structures are made of brittle material. In the initial phases, especially when considering 3D structures, a "double peak" can be seen, which may be related to partial deformation of the cells or ligaments. However, the deformation of the whole structure has a significant meaning in the response to the load. In these cases, a small stress drop can be noted, but similarly to the aforementioned studies, only a meaningful deformation is visible as a significant drop in the stress curve.

Nevertheless, the wavy "plateau" may be generalised by the mean value approximating the transmitted loading. The mean values for plateau stresses (σ_{Pl}) are calculated based on the following equation:

$$\sigma_{Pl} = \frac{\int_{\varepsilon_{pl.}}^{\varepsilon_{den.}} \sigma(\varepsilon) d\varepsilon}{\varepsilon_{den.} - \varepsilon_{pl.}} \qquad (1)$$

Where $\varepsilon_{den.}$ Is the strain at the densification regime and $\varepsilon_{pl.}$ is the strain at the plateau regime.

The calculation of the mean stress has been described in detail in [1, 36].

The mean stresses for the quasi-statically compressed structure vary between 1.1 MPa (for the auxetic characterised by the lowest relative density among the tested structures) and 8.3 MPa (for the lattice, with the highest relative density). In the dynamic compression regime, the highest mean stress approximating the plateau of structural deformation characterises the lattice (14.2 MPa), further the foam (10.5 MPa), next

to the honeycomb (3.5 MPa) and the auxetic (1.4 MPa). The mean stresses calculated for the dynamic compression are 30–40 % higher than those characteristic for the quasistatic tests. They are also much higher for the structures built with 3D cells than for the 2D ones.

In the quasistatic compression, all studied structures show that the first distinctive peak corresponds to a large elastoplastic deformation, followed by the breakage of cell bonds, Fig. 4. The structures are deformed in about 10–15 % when the collapse starts. The deformation starts from the upper surface for the honeycomb, auxetic, and lattice structures; for the foam, it starts from the bottom. The inward collapse, typical for the metamaterials with a negative Poisson's ratio [16,17,38, 39], also characterises the tested AM auxetic. The buckling at the quasistatic strain rate corresponds to an almost constant force level throughout the compression of the auxetic structure. The observed lattice deformation is featured by the concentration of stresses leading to a localised shearing that becomes apparent after 30 % of the deformation.

The studied structures' dynamic responses differ from those of the quasistatic ones. Figs. 6(a–b) show that in the initial stage of the deformation (5 %), stretching the cells outwards is observed for the honeycomb and auxetic. Further, the HS camera registered that the cells of tested 2D structures collapsed inward to the structures' centres. At 30 % of deformation, the synclastic curvature of the deformation features a "dome-shape" damage mode for both 2D structures. Figs. 6(c–d) show that the lattice and foam have similar deformation mechanisms in the initial deformation stage, up to 10 % of the strain. The lattice is characterised by bending the cells' struts and stretching the whole structure, Fig. 6(c). The deformation process ends due to shearing the entire structure. In the case of the foam structure Fig. 6(d), the shearing mode of the deformation occurs after 10 % of strain.

The specimens with 3D geometry absorbed all energy transmitted by the blast wave; therefore, the stress curves dropped to zero in Fig. 3(b). It is worth noting that the foam structure had to undergo much more deformation than the lattice to transfer the same amount of force. On this basis, the lattice is expected to have a higher specific energy absorption, which will be discussed in the following paragraph.

Table 4, which summarises the peak and mean stress values and the densification strain, shows differences in the calculated characteristics for the quasistatic and dynamic processes. The values of the peak stresses are 9 % (for the lattice: 19.6 MPa in the quasistatic and 21.6 MPa in the dynamic range)and 39 % (for the auxetic: 1.1 MPa and 1.8 MPa, respectively) lower in the quasistatic compression. Similarly, the mean stresses, which at the quasistatic deformation rate are 22 % and 57 % lower than in the dynamic range (for the auxetic: 1.1 MPa in the quasistatic and 1.4 MPa in the dynamic range and for the honeycomb: 1.5 MPa and 3.5 MPa, respectively). The densification strain is almost the same for the honeycomb in both strain rate regimes (it is measured as 0.8 for both compression types). However, it is almost 50 % higher in the quasistatic range for the 3D structures (0.3 and 0.8 for the dynamic and quasistatic compression lattice, whereas for the foam, the strain was measured as 0.5 and 0.8 in the dynamic and quasistatic compression).

Differences in the structural response under static and dynamic load may originate from several reasons. Depending on the material's loading conditions, inherent characteristics, and the structure itself, the additively manufactured structures may behave differently under quasistatic and dynamic compression. First, similarly to conventional aluminium, the additively manufactured aluminium displays differences in mechanical characteristics and material properties due to the strain rate sensitivity. Because of the manufacturing process's internal imperfections and voids, the AM material may undergo stronger microstructural changes in the rapid deformation of the blast-induced compression. Moreover, inertia effects, which are not dominant in a quasistatic deformation, may significantly impact how structures react to dynamic loadings. Dynamic wave propagation can also affect stress concentration and deformation patterns. Finally, the rate at which energy is dissipated during deformation can affect the overall response of the tested cellular structures. The energy absorption mechanisms may differ in the

Table 5
Stress ratio (SR) of quasi-static and dynamic compression regimes.

$SR = \dfrac{\sigma_{Pl\ Blast}}{\sigma_{Pl\ QS}}$	Lattice	Foam	Honeycomb	Auxetic
	1.61 ± 0.1	1.05 ± 0.27	1.97 ± 0.27	1.07 ± 0.2

quasistatic and dynamic compression, leading to different failure modes. The next section concerns the discussion on the energy absorption capacity of the tested structures.

4.1. Energy absorption characteristics

Compared to the 2D structures, the structures characterised by 3D unit cells demonstrate a significant leap in energy absorption (EA) capacity, as illustrated in Fig. 7. The absorbed energy dependences [3,31,36,38,39], calculated using Eq. (2) and presented in Fig. 7, reveal that the foam and lattice structures can reach about 180 J of the EA parameter (in the quasistatic compression) and 160 J (in the blast-induced compression). The EA values for the honeycomb and auxetic structures are about 37 J and 21 J for the slower compression and 78 J and 27 J for the dynamic process. Notably, with its longer compression process, the honeycomb structure leads to the highest densification stroke efficiency, up to 15 %, in dynamic and quasistatic compression.

$$EA = \int_0^{x_d} F_{trans}(x)dx \qquad (2)$$

where $F_{trans}(x)$ is the registered force, x is the reduction of the sample height during compression, *and* x_d is the value of sample deformation at the onset of the densification process.

The results obtained from the performed quasistatic and dynamic tests may also be referred to each sample's mass using the specific energy absorption parameter. Such a parameter requires that the whole sample has been crushed, which is not the case in the analysed dynamic compression, where the experimental setup limits the amount of energy brought to the sample. Therefore, the specific energy absorption (SEA) parameter was used, Eq. (3).

$$SEA = \frac{EA}{V_0 - V} = \frac{\int_0^{x_d} F_{trans}(x)dx}{V_0 - V} \qquad (3)$$

where EA is the absorbed energy, V_0 is the initial volume of the sample, V is the residual volume of the sample after the test, $F_{trans}(x)$ is the registered force, and x is the sample displacement during compression.

Compared to the 2D structures, the structures characterised by 3D unit cells demonstrate a significant leap in energy absorption capacity, as illustrated in Figs. 7–9. The absorbed energy dependences are calculated using Eq. (2) [38,39]. The energy in the elastic regime is also
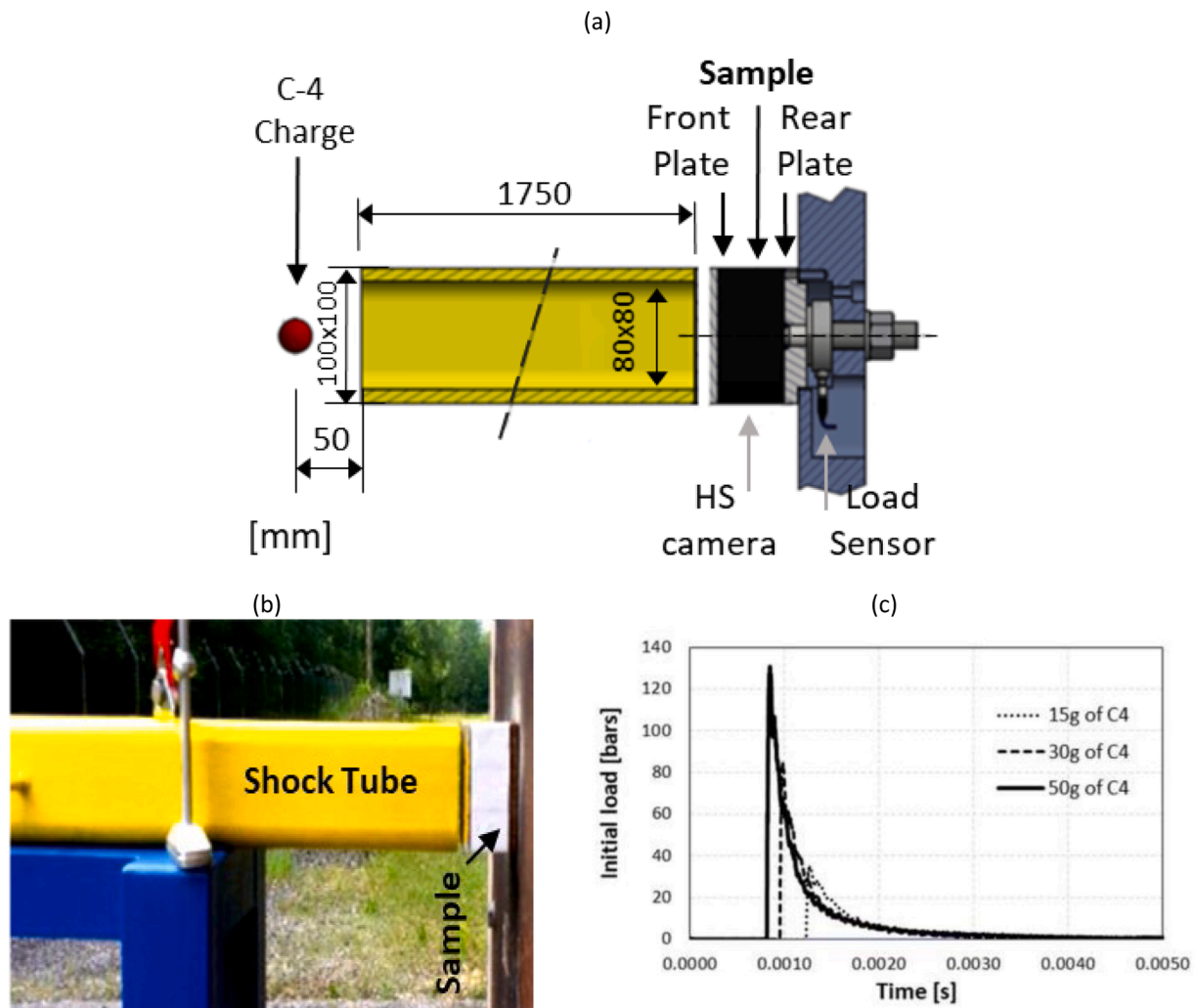
Fig. 5. Explosive-driven shock tube (EDST) setup: (a) scheme of the experimental configuration, (b) its picture, (c) loading profiles presenting measured blast wave pressures generated by detonation of C-4 charges with different masses.
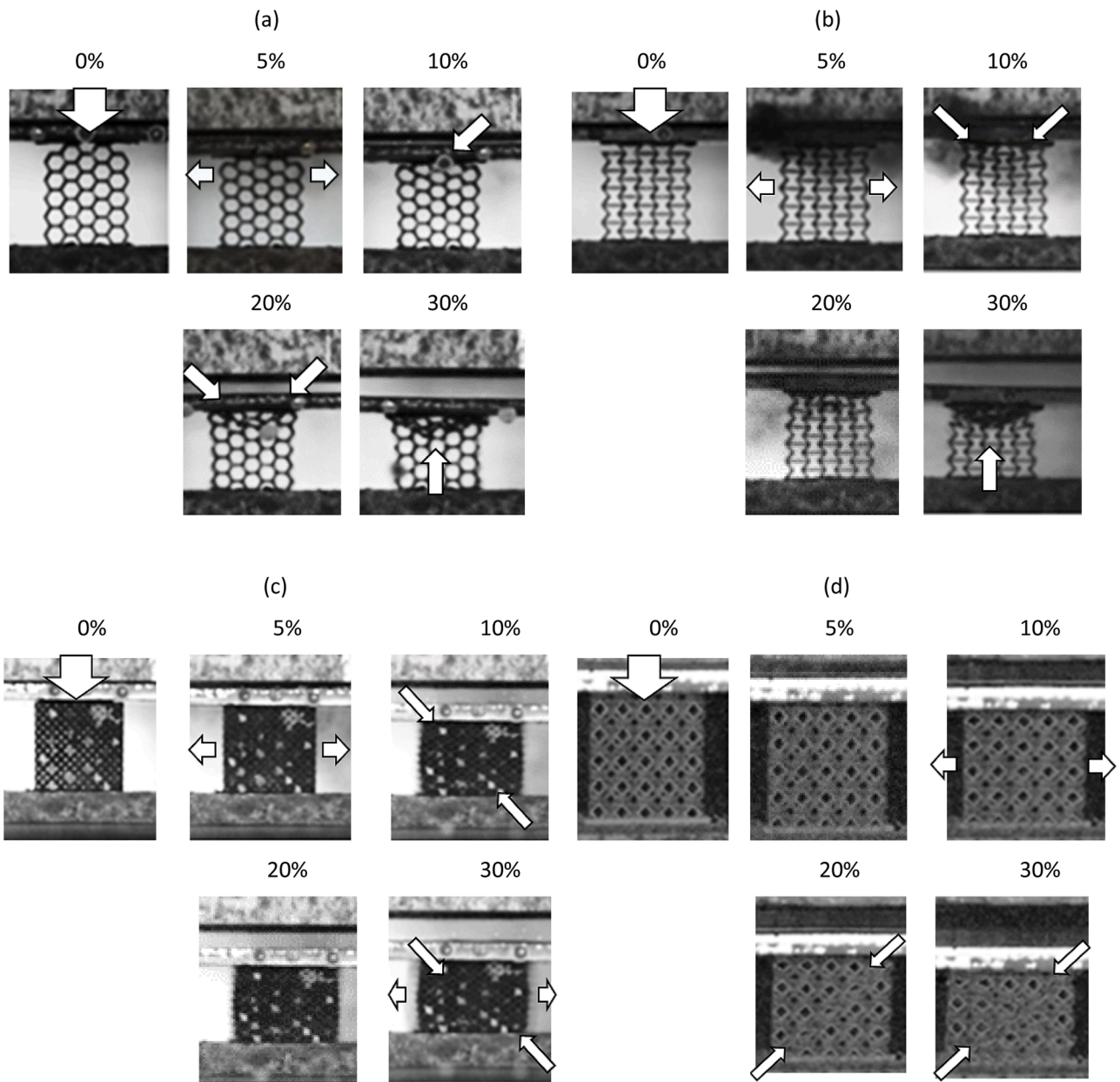
Fig. 6. Subsequent phases of the blast-induced compression of (a) honeycomb, (b) auxetic, (c) lattice and (d) foam structures presented in the progress of deformation.

included in the overall result. However, its influence is negligible for metallic, brittle cellular structures and does not affect the final result by >5 %, as claimed also by [40,41]. It should be noted that the absorbed energy is counted till the densification regime.

The tangent of the curves shown in Fig. 7 may be directly related to the sample section, assuming it remained constant during the deformation. Such an approach enables the sample's energy absorption capability to be investigated at varying strain rates but similar levels of deformation. By doing so, it can be observed that the strain rate has a limited effect on the auxetic sample (< 5 %). However, it multiplies by two the energy absorption capacity of the honeycomb sample (from 37.5 J dissipated using 25 mm of honeycomb to 75 J (+ 100 %)). The foam is less responsive to the strain rate (+39 %) despite having a higher energy absorption capacity. Finally, the lattice structure has a high capacity for energy absorption and appears to be largely dependent on the strain rate effects (+100 %). When compared altogether, and by taking into account the initial relative density of each sample, the structures

characterised by the 3D unit cells present the highest specific energy absorption capacity, which shows that they are better absorbers of energy absorbed per unit mass.

Equation 43 concerns the stress ratio (SR) in dependence on the strain rate of the compression loading and the mean plateau stress. Following the definition of the parameter, Table 5 concludes on the structures' sensitivity to strain rate changes. The parameter SR shows that the honeycomb and lattice structures are more sensitive (almost two times) to strain rate changes than the auxetic and foam structures.

$$SR = \frac{\sigma_{Pl\ Blast}}{\sigma_{Pl\ QS}} \tag{4}$$

where $\sigma_{Pl\ Blast}$ and $\sigma_{Pl\ QS}$ are the average values of the plateau stress in the blast and quasistatic regimes, respectively.

The curve slopes, Fig. 8, indicate differences between the two strain rate regimes. It is seen that the lattice is characterised by the highest slope, which is equal to 0.0074, then the foam (0.0032) and the
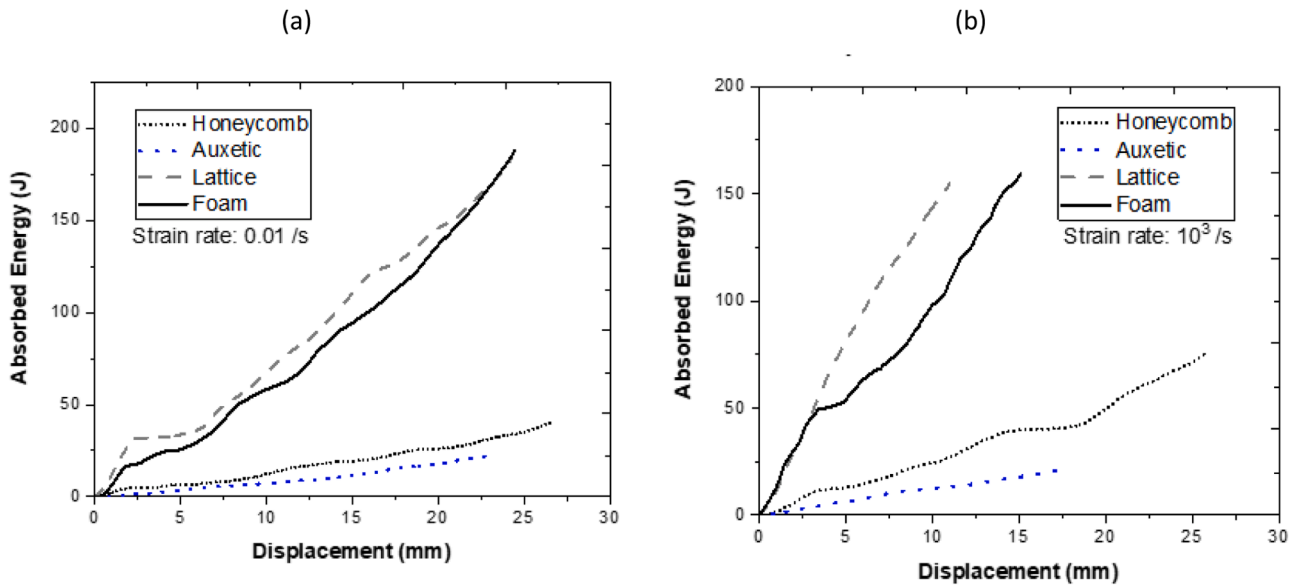
(a)

(b)

Fig. 7. Absorbed energy in the structures' displacement for (a) quasi-statically and (b) dynamically compressed AlSi10Mg structures.
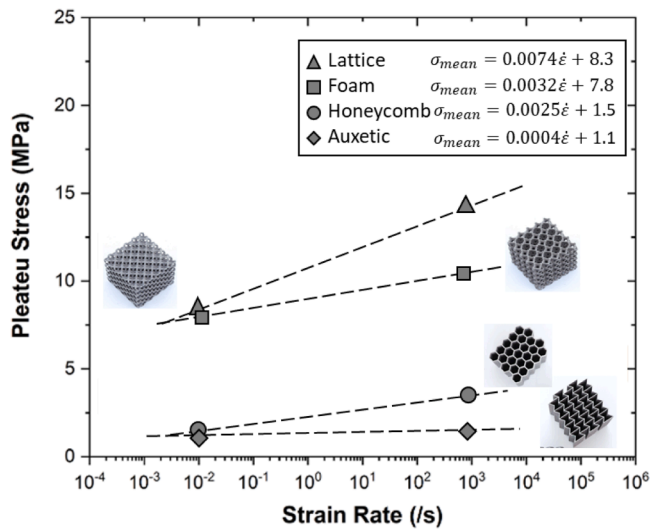

Fig. 8. Slope of the mean stress curves in relation to the strain rate of compression loading characteristic for the tested AM structures.

honeycomb, featuring 0.0025. Wherein the slightest slope, equal to 0.0004, characterises the auxetic. Therefore, increasing the strain rate enlarges a structure's ability to transfer the loading force. The findings also underscore the better energy absorption efficiency of the 3D structures compared to their 2D counterparts. When exposed to the same blast wave, the tested 3D structures can enhance absorption efficiency up to three times compared to the tested 2D structures. In addition, the absorption efficiency of 3D structures is not significantly dependent on the direction of force application. It is also observed that the auxetic structure achieved the lowest energy absorption capacity with its negative Poisson coefficient. However, its stroke efficiency is nearly twice as low as the honeycomb's. This conclusion should be drawn assuming that the relative density of the examined structures is the same, whereas its values are 0.15 and 0.17 (for the auxetic and honeycomb) and 0.19 and 0.21 (for the foam and the lattice).

The recorded deformation and collapse of the tested samples and the registered stress-strain responses prove that each cell configuration's failure mode differs. Enlarging the analysis by numerical modelling of

the structural responses to the dynamic loading provides further insight into the observed mechanisms.

5. Numerical approach

5.1. Numerical configuration

The numerical simulation of the blast compression tests is developed in the explicit LS-DYNA solver, ver. R9.0.1. The objective of the simulation is to model the behaviour of the AM structures compressed dynamically in the EDST test. Therefore, as shown in Fig. 9, the numerical task simplifying the experimental setup consists of the solid parts representing the tested sample placed between two steel plates (8 $\times$ 100 $\times$ 100 mm^3 and 11 $\times$ 100 $\times$ 100 mm^3). The tested structures' complex geometries were modelled in a CAD program and then meshed, applying the Lagrange approach in the Ls-PrePost [42,43]. As the measured wall thicknesses vary, an average value of 0.5 mm is considered in the calculations. The load is assigned to the nodes of the upper surface of the front plate. The pressure profiles presented in Fig. 5(b) are implemented to the numerical task as the initial load. The pressure data were taken from the test in which 30 g of C4 was detonated without an absorbing structure. The initial force recalculated from such a pressure loading is distributed to nodes of the upper surface of the front plate on the area equal to the inner tube cross-section; see for the detailed explanations [33]. The load profile is a crucial initial condition that imposes displacement of the front plate. The contact between the components is ensured by the option *AUTOMATIC_SURFACE_TO_-SURFACE. The bottom surface of the rear plate is fully constrained, similar to the experimental conditions. The friction coefficient between the interacting components is assumed to be 0.5 [44].

The lattice consists of 1.407.277 elements (1.952.500 nodes), the foam of 1.784.010 elements (1.859.500 nodes), whereas the honeycomb and the auxetic of 1.167.260 and 1.266.300 (1.502.157 and 1.687.084 nodes), respectively. The used elements are the default constant-stress solid element type. The 2D structures are meshed by cuboid elements, whereas the more complex 3D geometries are meshed by tetrahedron elements. The elements' edge length varies between 0.15 mm and 0.35 mm.

5.2. Material model

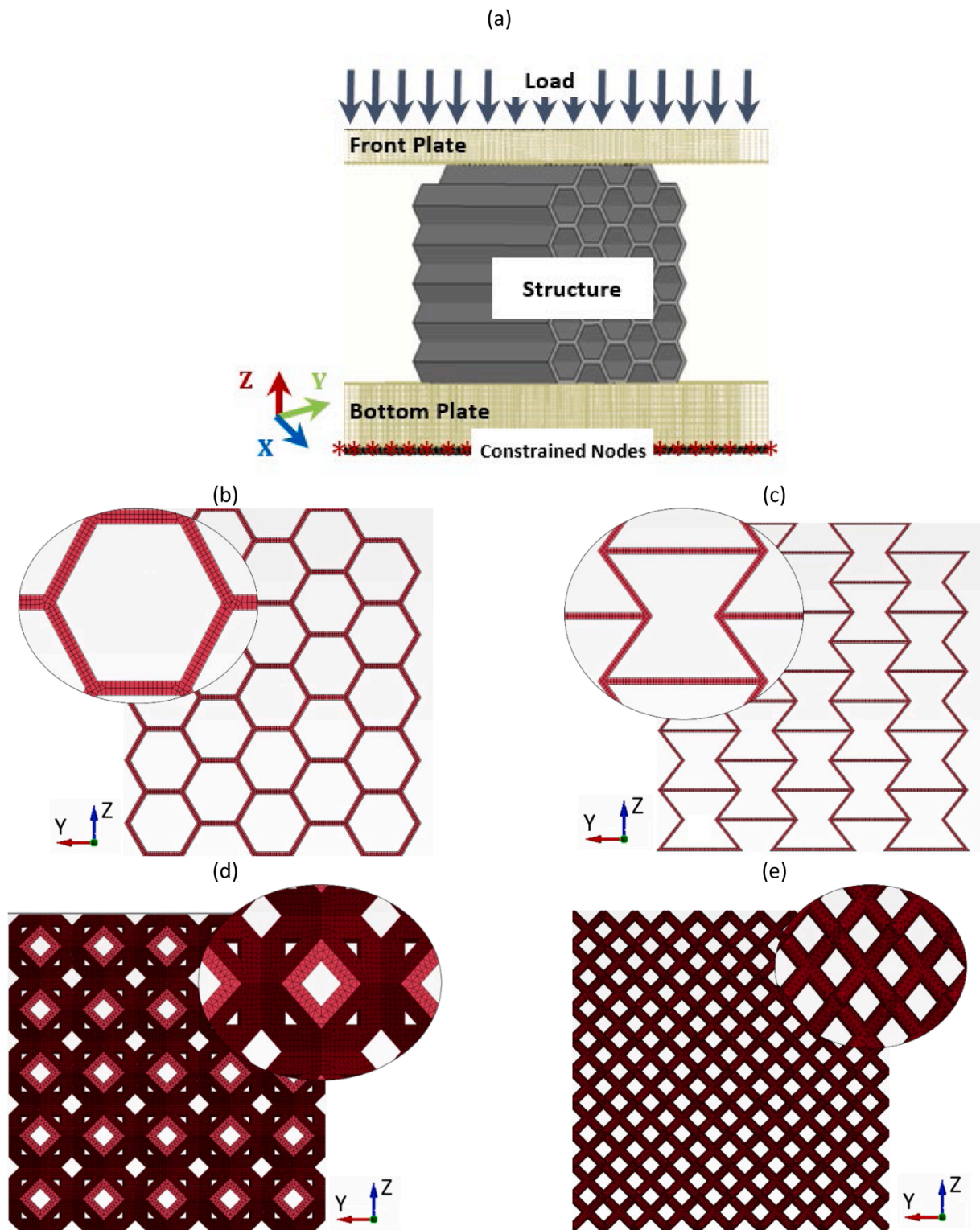The *MAT_024 (Piecewise_Linear_Plasticity) was chosen to represent

Fig. 9. Numerical configuration of the EDST blast test (a). Meshes of: (b) honeycomb, (c) auxetic, (d) foam, (e) lattice.

the behaviour of the AlSi10Mg aluminium alloy. The results of the quasi-statistic and dynamic compression obtained using the Split Hopkinson Pressure Bar test, conducted to characterise the behaviour of the printed material in the as-built state, are compiled in Fig. 10. The compression tests, performed at varying strain rates from 0.001 s⁻¹ to 3300 s⁻¹ and temperatures up to 200 °C, provide an overview on the material's performance. A detailed discussion of the material characterisation and the modelling approach is presented in the precedent study [33,36]. The

performance of the compressed cylindrical samples extracted in three build directions and tested at various strain rates and temperatures is summarised and used to define the material behaviour in the numerical simulation [45].

The quasistatic compression tests were performed using cylinders with dimensions 6 mm (diameter) and 9 mm (height). In the dynamic compression tests performed using the Split-Hopkinson Pressure Bars, the cylindrical samples of diameter and height 6 mm and 3 mm were
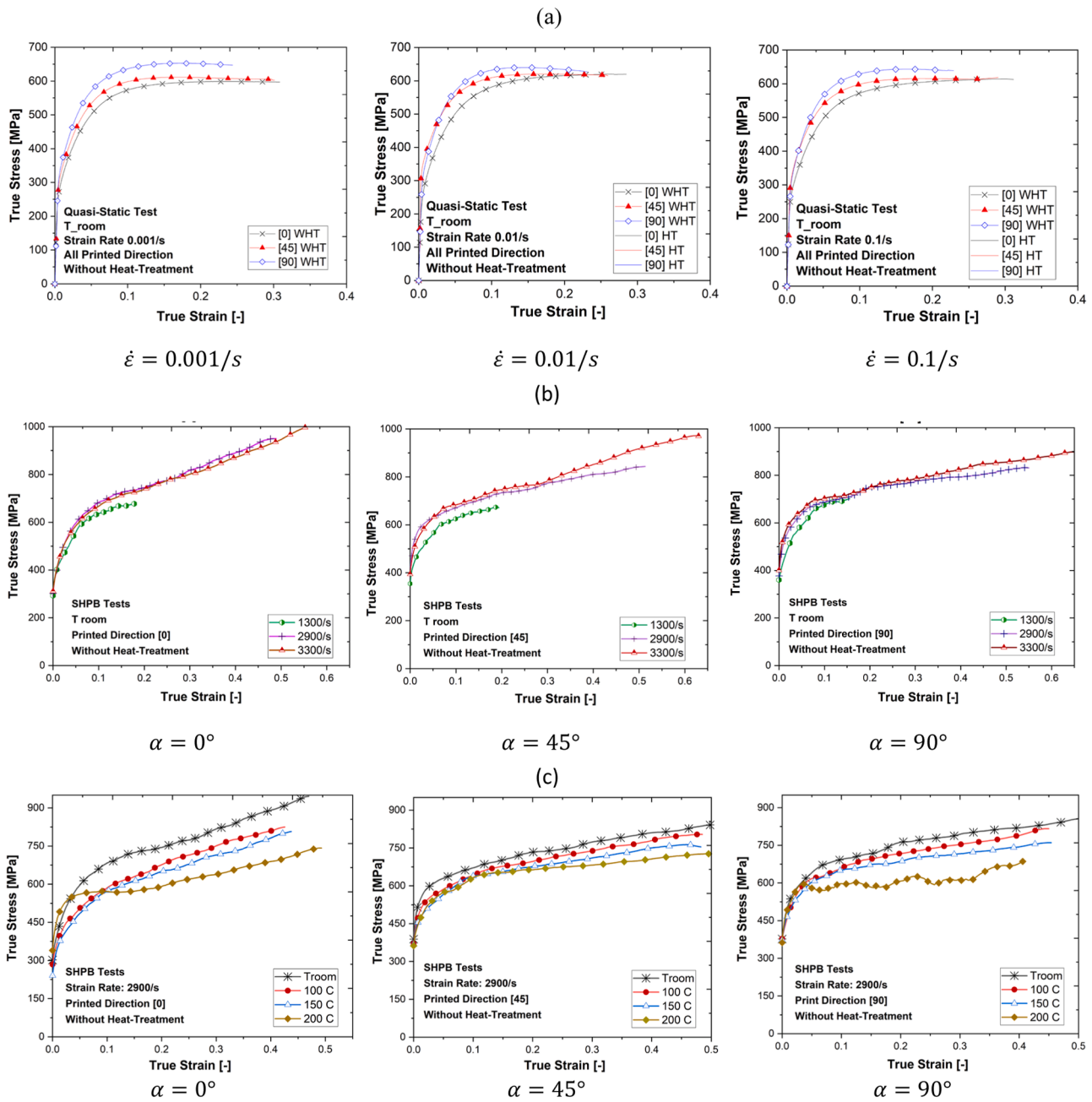
Fig. 10. Characterization of the AlSi10Mg 'as-fabricated': (a) quasi-static compression, (b) SHPB compression, (c) temperature influence.

tested to increase the maximum strain rate. To verify the effects of the material anisotropy, the specimens for compression tests were printed in three directions – the horizontal print [0°], vertical [90°] and at the angle of 45° to the build platform. This approach follows the assumption of transversal isotropy of the printed material. For each printed direction, the values of the true stress at the true strain of 0.1 are collected in Fig. 11(a).

Based on the results, the additively manufactured AlSi10Mg aluminium is almost unaffected by the strain rate changes at quasistatic conditions. However, the material hardens significantly in dynamic ranges along with the increase of imposed compressive strain rates. The orientation of the sample to the built platform influences the stress-strain results more significantly—the differences in the plastic stress values measured at the strain of 0.1 vary by 80 MPa, Fig. 11(b-d). In the as-printed conditions and the quasistatic range, the highest level of stresses, about 640 MPa, presents the material printed at [90°] to the

building platform. It is proceeded by the material printed at [45°], for which the average level of the stresses is close to 605 MPa. The lowest material response features the samples printed at [0°] – its average in quasistatic conditions is 560 MPa. It is also shown that the hardening stage occurs at lower stress values with the temperature increase. The highest temperature sensitivity is noticed for the horizontally printed samples [0°], whereas the lowest is registered for the samples printed at an angle of [45°]. Compared to the quasistatic tests, an increase in the isothermal test conditions at dynamic rates causes decreases in the obtained stress level. The values for tests of the samples printed in [0°], [45°] and [90°] are measured at 105 MPa, 40 MPa, and 95 MPa, respectively.

The material model is adjusted to the structure's position on the building platform and the experimental load direction. Therefore, the honeycomb and auxetic structures simulations are based on the characteristics obtained from the compression of the samples at an angle of
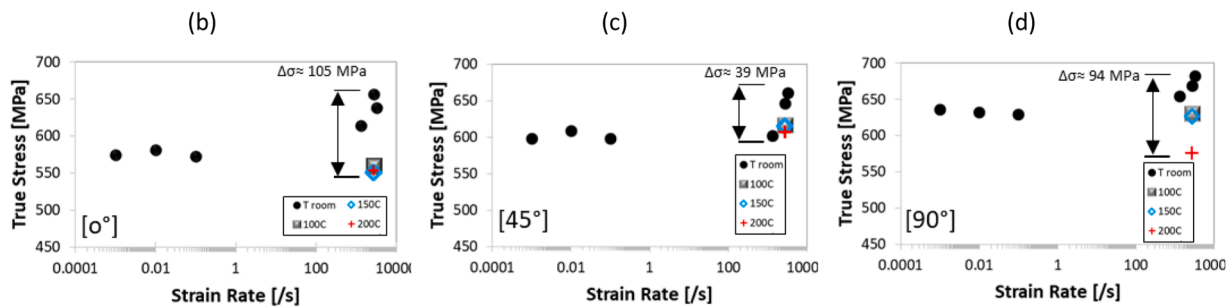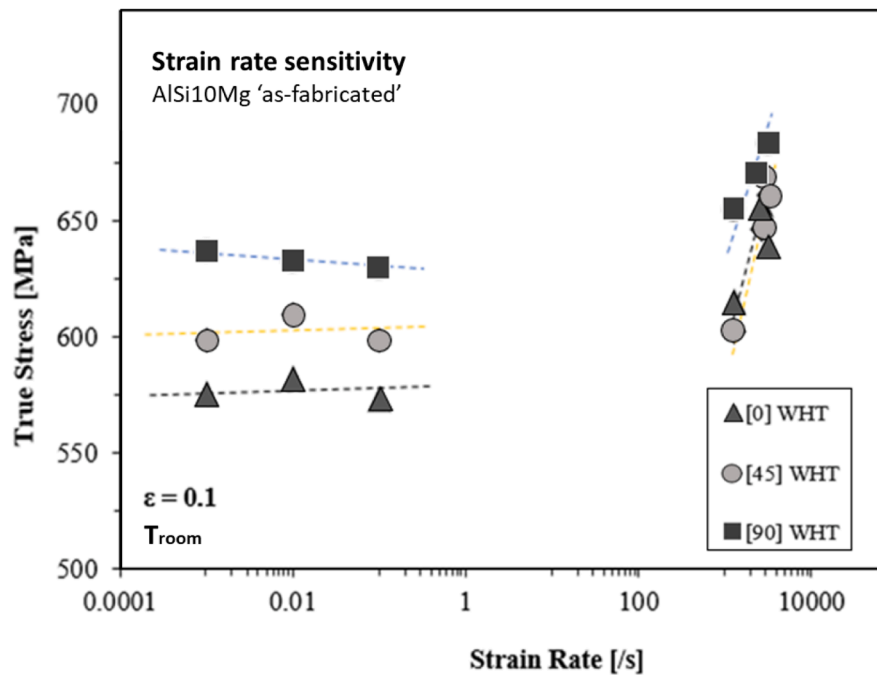
(a)

(b)   (c)   (d)

Fig. 11. (a) Strain-rate sensitivity for the 'AlSi10Mg 'as-fabricated', (b-c) temperature sensitivity.

[90°] and the lattice at an angle of [45°]. Depending on the wall position, the material characteristics of all three directions are used for the foam.

The failure condition of the maximum effective strain at failure with a value of 0.09, chosen based on the parametric study, is set to simulate the structures' brittle damage.

Based on the description discussed in [46,47], the model parameters for the steel plates are applied, employing the *MAT_098 (Simplified_Johnson_Cook) option, which accounts for the strain rate's influence on the material behaviour. No erosion condition is assumed for the plates' steel.

5.3. Numerical results

Fig. 12 compares the outcome of the simulations and experiments presenting the resulting equivalent stress-strain curves. Points "1," "2," and "3″ on the curves are correlated with suitable deformation mods that mark the characteristic phases observed in both the simulation and the blast experiments, as shown in Figs. 13–14.

Upon analysing the stress-strain curves resulting from the EDST experiment and its numerical simulation shown in Fig. 12, it may be remarked that the structures compressed numerically also exhibit the characteristic phases of cellular structure compressive deformation –

peak, plateau, and densification. Like in the experiment, each numerical curve course has fluctuations that can be correlated with the cell collapsing and the cell bond breaking. While a generally similar course of the experimental and numerical characteristics is observed, the detailed features differ, as summarised in Table 6. This contrast underscores the complexity of the progressive deformation and fracture of the cellular structures

Figs. 13 and 14 compare the experimentally and numerically obtained deformation and fracture paths of the compressed AM structures, revealing a good resemblance between the structural responses at each stage, which validates the numerical study. It is observed that the breaking of bonds occurs close to the cell vertexes in the 2D structures shown in Fig. 13. The honeycomb's cells are stretched in the upper part of the structure, causing the progressive movement of further cells along with the deformation. A similar, orderly way of the cell collapse of the auxetic structure is combined with the folding towards the centre of the entire structure under the axial loading. Accordingly, the middle cells prove the elastic-plastic bends of their bases in opposite directions. Significant deformations occur at the cell vertexes, while the centre of the struts is almost not strained, the same as the upper and lower bases of each elementary cell.

The striped deformation mode also characterises the lattice structure, Fig. 14(a). Except for the first row, the strongest strains are visible
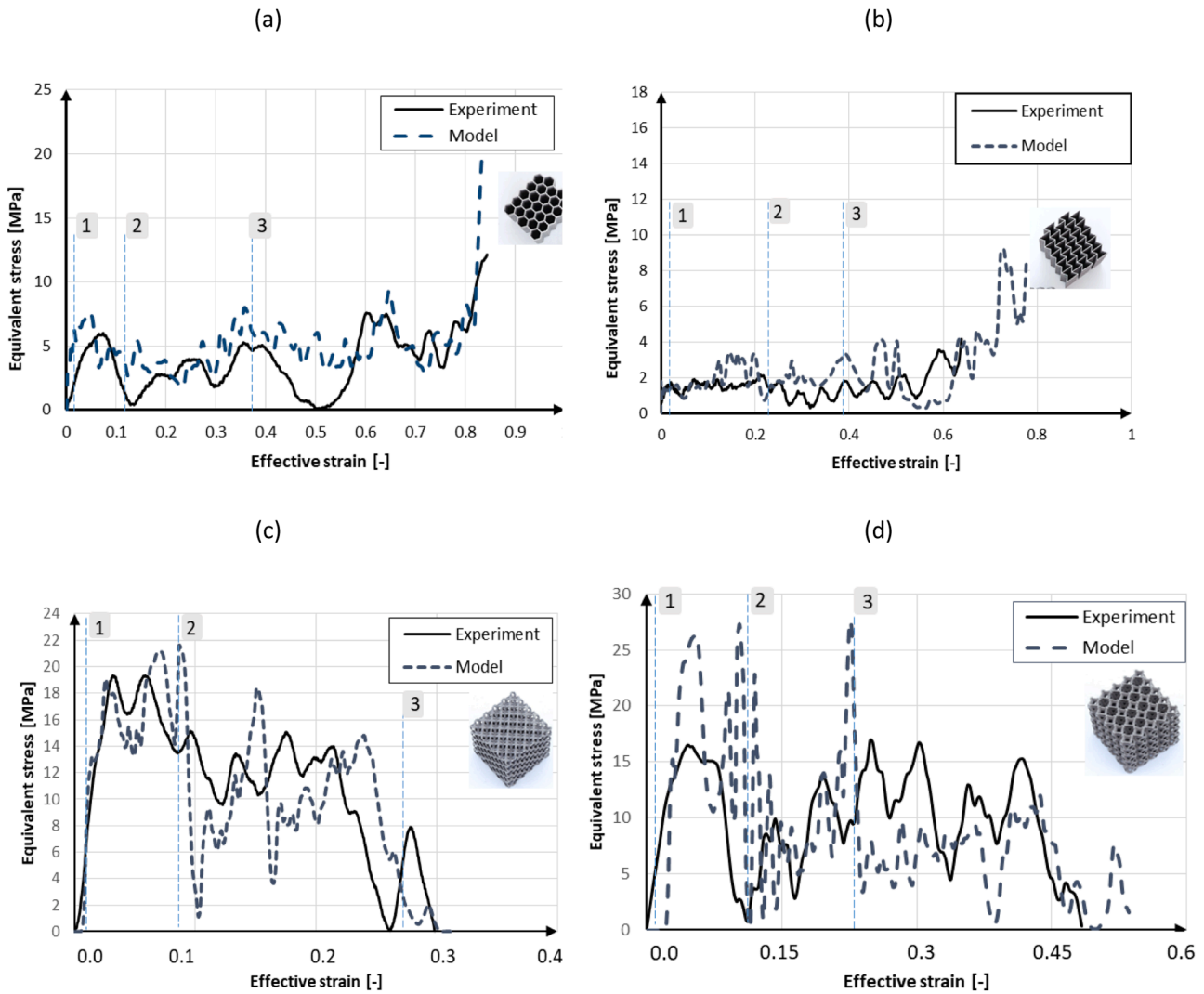
(a)

(b)

(c)

(d)

Fig. 12. Blast-induced compression of: (a) honeycomb, (b) auxetic, (c) lattice, (d) foam – comparison between the experimental and numerical results.

in each cell's centre, but the struts' centre is almost undeformed. The simulation indicates that the damage and eventual fracture occur in the struts, close to the centre of the whole cell. However, the bent struts met the struts from the cell below, which can prevent the bond breaks. Therefore, the lattice sample undergoes an extension of the entire structure – perpendicular to the load direction. Then, as the volume is lower and mass remains almost the same, the relative density increases.

Further, the global shearing is observed, and the deformation process is terminated. Fig. 14(b) shows the shear mode of the entire foam structure as it takes place also during the experiment. The detailed analysis indicates that the collapse mode of the foam is more complex than that of other tested structures. The deformation occurs between the nodes of the holes at each cell face and travels to the node on the next face. Therefore, the shear bands inside every single cell can be observed. In addition, the cell bases are almost undeformed, which is not the case for the cells of the 2D-type structures.

It should be noted that the idealised conditions in the simulation may omit some experimental features; thus, the numerical results differ from the experimental ones. The uneven plate load conditions, gravity's influence, or sudden air compression between the cells obviously cannot be accounted for in the simulation and may affect the experimental findings. It should be taken into account that the experimental measurements may also be affected by some errors due to the inaccuracy of the sensors or due to the filters used, which average the experimental force results. Lastly, defects in the real structures, internal voids,

roughness or print accuracy not represented in the current modelling also play a role in the onset of damage.

The error between the experimental and numerical results was calculated based on the formulation (5).

$$\text{Error} = \frac{\int_{\varepsilon_0}^{\varepsilon_d} \sigma_{exp}(\varepsilon)d\varepsilon - \int_{\varepsilon_0}^{\varepsilon_d} \sigma_{sim}(\varepsilon)d\varepsilon}{\int_{\varepsilon_0}^{\varepsilon_d} \sigma_{exp}(\varepsilon)d\varepsilon} * 100\% \quad (5)$$

The errors between the numerically and experimentally obtained curves are collected in Table 7.

Generally, two key reasons behind running a simulation are understanding an analysed loading scenario and/or facilitating further prototyping of structures made with the analysed material. It should be kept in mind that the blast and ballistic testing are very fast tests, lasting only a few micro/milliseconds, and their analysis relies on a restricted range of in-situ observations. In these conditions, numerical simulation is another tool for observing and analysing the experiment. A proper setting of the numerical configuration, BC, material model calibration, validation, etc., is valid as for any other numerical task. Our simulation has enabled us to achieve the primary objective: a thorough analysis of the experimental results. The simulation accurately replicated the failure mechanism for each structure, providing insight into the progressive collapse of each cell type. A detailed visualisation of the blast-induced deformation of the tested structures supports further analyses if required. The performed simulations allowed a detailed analysis of
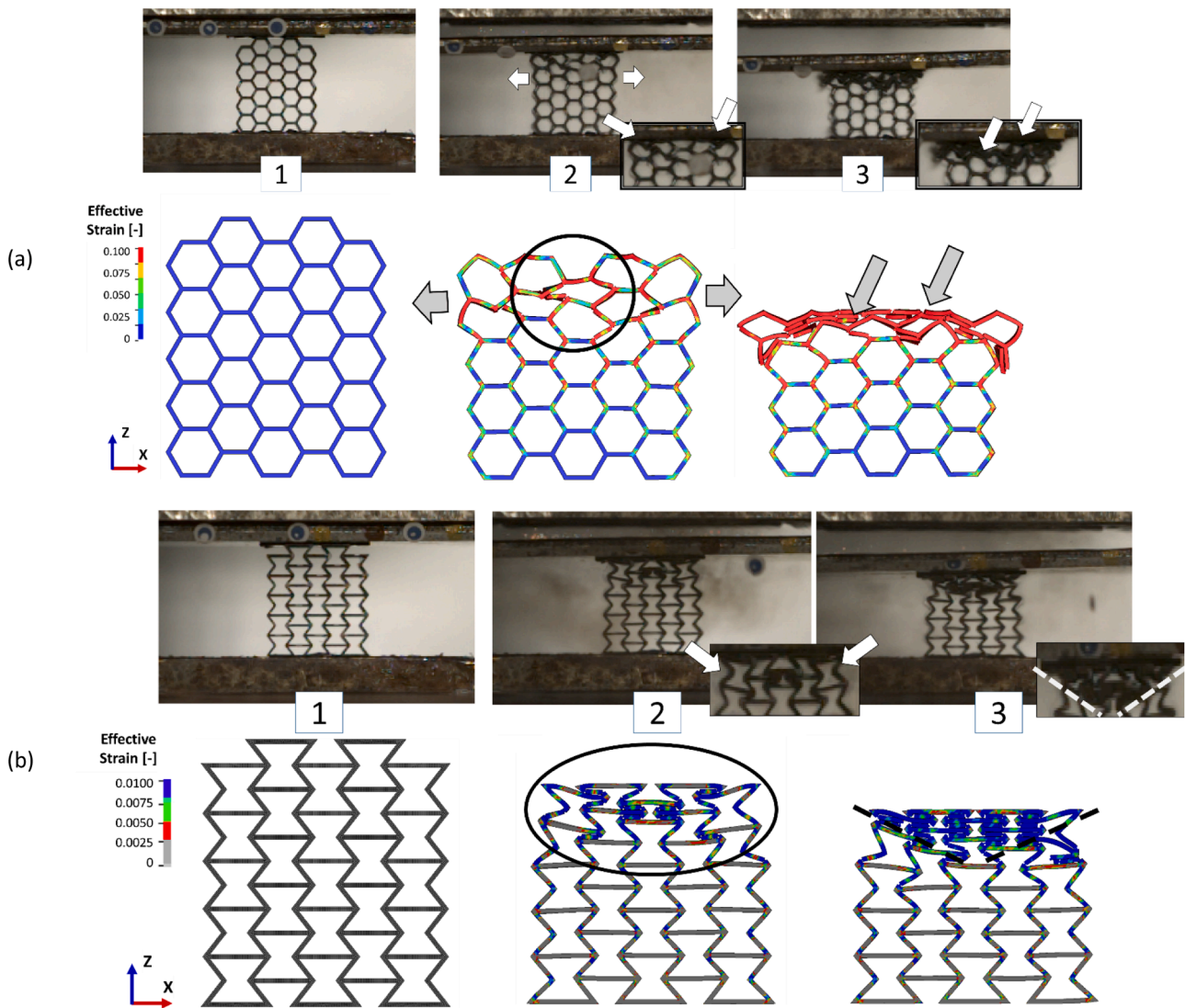
Fig. 13. Comparison between the experiment and numerically obtained failure modes resulted from the blast-induced compression of: (a) honeycomb, (b) auxetic.

deformation modes, indicating the stress concentration and providing insight into each structure's deformation paths. It has been observed that the stretching of the cells characterises the honeycomb outwards and the auxetic structure by folding the cells towards their centre. The bending of the struts is visible for the lattice structure, and the foam is characterised by the deformation mechanism between two vertexes of the cell. Moreover, the numerical results specify non-strained areas for each structure, whose removal should not change the mechanism of the blast energy absorption but may improve the SEA parameter. The performed numerical simulation provided a verified basis for the future prototyping of cellular structures of different geometries printed with the AlSi10Mg alloy.

6. Conclusions

This paper analyses the absorptive properties of the AlSi10Mg 3D and 2D structures, such as a honeycomb, auxetic, lattice and foam of a similar relative density, manufactured additively and tested in as-printed conditions. The structures were compressed quasi-statically and dynamically under a blast loading generated in an explosively driven Shock Tube setup. The performed investigation proves that the structural topology considerably influences the material response to compressive loadings. The structures characterised by 3D unit cells

(foam and lattice) compared to those with 2D unit cells (honeycomb and auxetic) demonstrated up to six times higher mean stress under the quasistatic compressive loading. This difference is greater under dynamic compression. The analysis shows that higher strain rates of the loading increase the stress level in the crushed sample and affect the damage modes of the collapsing structure. The strain rate analysis proved that the highest ratio of the obtained stress characterises the honeycomb and lattice structures in the quasistatic and dynamic regime.

An explicit numerical simulation further analysed the blast-induced deformations of the AM cellular structures. The implemented material model was based on the detailed characterisation of the AM bulk material in a wide strain rate and temperature range. The material characterisation showed that the building direction and heat treatments affect the material' yield stress and elasticity modulus. These effects were accounted for in the material modelling used by the numerical simulation. The computational results showed that the cells stretch outwards under the dynamic compression in the honeycomb structure, whereas in the auxetic, the cells fold towards their centre. In the lattice, the structure collapse is caused by the bending of subsequent struts rows, and in the foam structure, the damage mode contains deformation of the cells' vertexes. A comparison between the experimental and numerical results of the dynamically compressed AM structures shows a good resemblance, which validates the applied approach.
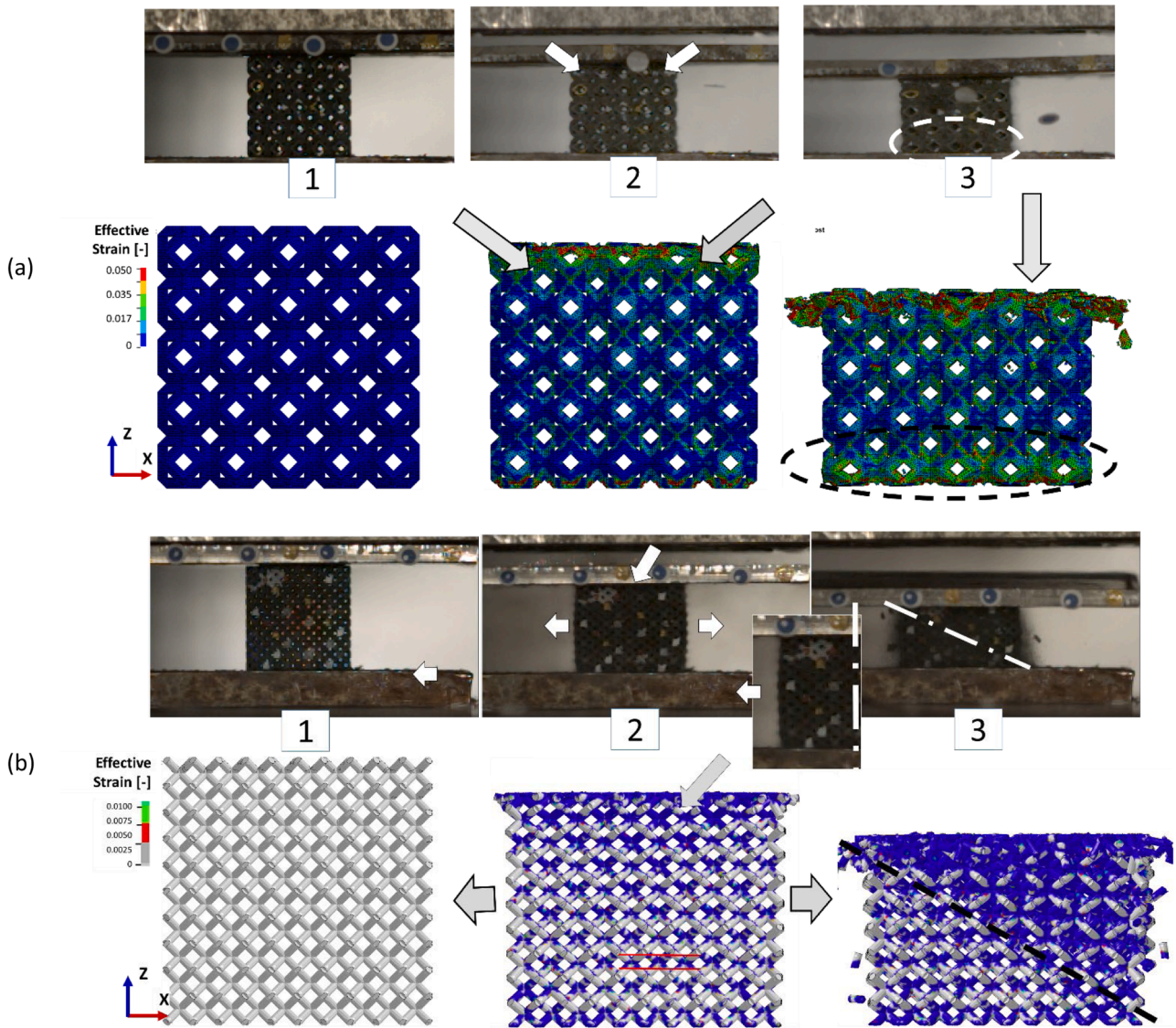
Fig. 14. Comparison between the experiment and numerically obtained failure modes resulted from the blast-induced compression of: (a) lattice and (b) foam.

Table 6
Numerically obtained characteristics of the blast-compressed AM structures along with the accuracy percentage relative to the experiment.

	Lattice		Foam		Honeycomb		Auxetic	
Peak stress [MPa]	19.26	*11 %*	26.13	*50 %*	8.15	*36 %*	1.82	*4 %*
Mean stress [MPa]	12.48	*12 %*	15.6	*49 %*	5.72	*63 %*	2.62	*82 %*
Densification strain [-]	0.27	*13 %*	0.58	*12 %*	0.82	*2 %*	0.79	*36 %*

Table 7
Error between the experimental and numerical curves based on the Eq. (4).

	Honeycomb	Auxetic	Lattice	Foam
Error	31.51 %	19.03 %	37.9 %	43.85 %

The findings of this study may have implications for the design of additively manufactured metallic structures. The research highlights the potential of 3D structures to be optimised as lightweight metamaterials.

The experimental-numerical study performed provides insights into structural damage under a fast, crushing load. The results can guide further research on the geometry optimisation of structures attenuating explosive and shock waves, paving the way for further optimisation of additively manufactured structures with similar absorptive properties but a lower mass.

Author agreement statement

We the undersigned declare that this manuscript is original, has not been published before and is not currently being considered for publication elsewhere.

We confirm that the manuscript has been read and approved by all named authors and that there are no other persons who satisfied the criteria for authorship but are not listed. We further confirm that the order of authors listed in the manuscript has been approved by all of us.

We understand that the Corresponding Author is the sole contact for the Editorial process. He/she is responsible for communicating with the other authors about progress, submissions of revisions and final approval of proofs

Signed by all authors as follows:

CRediT authorship contribution statement

Piotr Pawlowski: Writing – review & editing, Writing – original draft, Methodology, Investigation, Conceptualization. **Magda Stanczak:** Writing – original draft, Resources, Investigation, Data curation. **Paula Broniszewska-Wojdat:** Writing – original draft, Investigation, Data curation. **Ludovic Blanc:** Writing – review & editing, Writing – original draft, Investigation, Data curation. **Teresa Fras:** Writing – review & editing, Writing – original draft, Methodology, Funding acquisition, Conceptualization. **Alexis Rusinek:** Writing – review & editing, Writing – original draft, Supervision.

Declaration of competing interest

The authors declare that they have no known competing financial interests or personal relationships that could have appeared to influence the work reported in this paper.

Acknowledgements

Mr. Richard Bernier is thanked for performing material testing. We also thank Dr. Slim Bahi for the insightful discussions.

Data availability

No data was used for the research described in the article.

References

[1] Ebrahimi MS, Hashemi R, Etemadi E. In-plane energy absorption characteristics and mechanical properties of 3D printed novel hybrid cellular structures. J Mater Res Technol 2022;20:3616–32.
[2] Rusinek A, Zaera R, Forquin P, Klepaczko JR. Effect of plastic deformation and boundary conditions combined with elastic wave propagation on the collapse site of a crash box. Thin-Walled Struct 2008;46(10):1143–63.
[3] Gibson LJ, Ashby MF. Cellular solids: structure and properties. cambridge solid state science series. 2 edition. Cambridge University Press; 1997.
[4] Evans AG, Hutchinson JW, Fleck NA, Ashby MF, Wadley HNG. The topological design of multifunctional cellular metals. Prog Mater Sci 2001;46(3–4):309–27.
[5] Abramowicz W, Jones N. Dynamic axial crushing of square tubes. Int J Impact Eng 1984;2(2):179–208.
[6] McFarland Jr RK. Hexagonal cell structures under post-buckling axial load. AIAA J 1963;1(6):1380–5.
[7] McFarland Jr RK. The development of metal honeycomb energy-618 absorbing elements. Jet Propulsion Laboratory California Institute of Technology 1964. Technical Report No. 32-639.
[8] Wierzbicki T. Crushing analysis of metal honeycombs. Int J Impact Eng 1983;1(2):157–74.
[9] Wierzbicki T, Abramowicz W. On the crushing mechanism of thin-walled structures. J Appl Mech 1983;50:727–34.
[10] Yungwirth CJ, Wadley HN, O'Connor JH, Zakraysek AJ, Deshpande VS. Impact response of sandwich plates with a pyramidal lattice core. Int J Impact Eng 2008;35(8):920–36.
[11] Fleck NA, VS Deshpande. The resistance of clamped sandwich beams to shock loading. J Appl Mech 2004;71:386. ASME.
[12] Xue Z, Hutchinson JW. A comparative study of blast-resistant metal sandwich plates. Int J Impact Eng 2004;30(1283).
[13] Mir M, Ali MN, Sami J, Ansari U. Review of mechanics and applications of auxetic structures. Adv Mater Sci Eng 2014;(1):753496.
[14] Chang Q, Jiang F, Yang S. Advanced honeycomb designs for improving mechanical properties: a review. Compos: B Eng 2021;227:109393.
[15] Velea MN, Lache S. In-plane effective elastic properties of a novel cellular core for sandwich structures. Mech Mater 2011;43(7):377–88.
[16] Yang Y, Fallah AS, Saunders M, Louca LA. On the dynamic response of sandwich panels with different core setups subject to global and local blast loads. Eng Struct 2011;33(10):2781–93.
[17] Mehreganian Navid, Fallah AS, Sareh P. Structural mechanics of negative stiffness honeycomb metamaterials. J Appl Mech 2021;88(5):051006.
[18] Liu N, Mehreganian N, Sareh P. Never better than 5/6: the fundamental limit of energy absorption efficiency for negative-stiffness curved-beam honeycombs. Mater Des 2024;243:113024.
[19] Chen Y, Ye W, Shi P, He R, Liang J, Feng J, Sareh P. Computational parametric analysis of cellular solids with the miura-ori metamaterial geometry under quasistatic compressive loads. Adv Eng Mater 2023;25(16):2201762.
[20] Moghaddam NS, Jahadakbar A, Amerinatanzi A, Elahinia M. Recent advances in laser-based additive manufacturing. In: Bian L, Shamsaei N, Usher JM, editors. Laser-based additive manufacturing of metal parts: modeling, optimisation, and control of mechanical properties. Boca Raton: CRC Press by Taylor & Francis Group; 2018. p. 1–23.
[21] Kruth JP, Dadbakhsh S, Vrancken B, Kempen K, Vleugels J, Humbeeck JV. Additive manufacturing of metals via selective laser melting process aspects and material developments. In: Srivatsan TS, Sudarshan TS, editors. Additive manufacturing innovations, advances, and applications. Boca Raton: CRC Press by Taylor & Francis Group; 2016. p. 69–96.
[22] Saheb SH, Durgam VK, Chandrashekhar A. A review on metal powders in additive manufacturing. AIP Conf Proc 2020;2281(1).
[23] Cooke A. and Slotwinski J. Properties of metal powders for additive manufacturing: a review of the state of the art of metal powder property testing, 809–88, 2012.
[24] Gite RE, Wakchaure VE. A review of process parameters, microstructure and mechanical properties of additively manufactured AlSi10Mg alloy. Mater Today: Proc 2023;72:966–86.
[25] Logakannan KP, Ruan D, Rengaswamy J, Kumar S, Ramachandran V. Fracture locus of additively manufactured AlSi10Mg alloy. Thin-Walled Struct 2023;184:110460.
[26] Ghisi NB, Ramos H, Kindleyside L, Aboulkhair NT, Santiago R. The influence of the characteristic microstructure of additively manufactured AlSi10Mg on the plastic behaviour at various strain rates. Mater Des 2022;223:111112.
[27] Wei Y, Zhang C, Yuan Y, Chen P, Huang C, Li J, Yuan M. Blast response of additively manufactured Ti–6Al–4V sandwich panels. Int J Impact Eng 2023;176:104553.
[28] Dharmasena KP, Wadley HN, Williams K, Xue Z, Hutchinson JW. Response of metallic pyramidal lattice core sandwich panels to high-intensity impulsive loading in air. Int J Impact Eng 2011;38(5):275–89.
[29] Harris JA, Winter RE, McShane GJ. Impact response of additively manufactured metallic hybrid lattice materials. Int J Impact Eng 2017;104:177–91.
[30] Ramos H, Pickering E, AlMahri S, Krishnan K, Oyebanji J, Guan Z, Langdon G, Santiago R. Experimental evaluation of hybrid lattice structures subjected to blast loading. Addit Manuf 2023;76:103751.
[31] Blanc L, Lebaillif D, Bufalo; A. Experimental analysis of fluid-structure interaction between a blast wave and a sandwich add-on armour. AIP Adv 2022;12(5):055105. 1 May.
[32] Stanczak M, Rusinek A, Broniszewska P, Fras T, Pawlowski P. Influence of strain rate and temperature on the mechanical behaviour of additively manufactured AlSi10Mg alloy. B Pol Acad Sci-Tech 2022;70(4).
[33] Stanczak M, Fras T, Blanc L, Pawlowski P, Rusinek A. Blast-induced compression of a thin-walled aluminum honeycomb structure—experiment and modeling. Metals (Basel) 2019;9(12):1–24. 1350.
[34] Stanczak M, Fras T, Blanc L, Pawlowski P, Rusinek A. Numerical modelling of honeycomb structure subjected to blast loading. In: Proceedings of the 12th European LS-DYNA Conf, Koblenz, Germany; 2019.
[35] Stanczak M, Fras T, Blanc L, Pawlowski P, Rusinek A. Numerical and experimental study on mechanical behaviour of the AlSi10Mg aluminium structures manufactured additively and subjected to a blast wave. EPJ Web Conf 2021;250.
[36] Stańczak M. Behaviour of additively manufactured metallic structures under blast loading. Diss. Université de Lorraine; 2022.
[37] "EOS_Aluminium_AlSi10Mg" Status 01/2022 [Online] https://www.eos.info/en-us/metal-solutions/metal-materials/aluminium#eos-aluminium-alsi10mg [Accessed 20.06.2024].
[38] Li QM, Magkiriadis I, Harrigan JJ. Compressive strain at the onset of densification of cellular solids. J Cell Solid 2006;42(5):371–92.
[39] Li J, Wei Y, Wu H, Shen X, Yuan M. Experimental crushing behaviour and energy absorption of angular gradient honeycomb structures under quasistatic and dynamic compression. Def Technol 2024;36:47–63.
[40] Ren X, Das R, Tran P, Ngo TD, Xie YM. Auxetic metamaterials and structures: a review. Smart Mater Struct 2018;27(2):023001.
[41] Mudassir M, Tarlochan F, Mansour M. Nature-inspired cellular structure design for electric vehicle battery compartment: application to crashworthiness. Appl Sci 2020;10:4532.
[42] Szachogluchowicz I, Sniezek L, Slezak T, Kluczyński J, Grzelak K, Torzewski J, Fras T. Mechanical properties analysis of the AA2519-AA1050-Ti6Al4V explosive welded laminate. Materials (Basel) 2020;13(19):4348.
[43] Fras T, Roth CC, Mohr D. Application of two fracture models in impact simulations. B Pol Acad Sci-Tech 2020;68(2):1–9.
[44] Javadi M, Tajdari M. Experimental investigation of the friction coefficient between aluminium and steel. Mater Sci - WROCLAW 2006;24(2/1):305.
[45] Pęcherski RB, Nalepka K, Fras T, Nowak M. Inelastic flow and failure of metallic solids. Material effort: study across scales. Constitutive relations under impact loadings: experiments, theoretical and numerical aspects. Springer; 2014. p. 245–85.
[46] Nemat-Nasser S, Amini MR, Choi RY, Isaacs R. Experimental and computational evaluation of compressive response of single and hex-arrayed aluminum tubes. J Mech Mater Struct 1910;2:2007.
[47] Fras T. Experimental and numerical study on a non-explosive reactive armour with the rubber interlayer applied against kinetic-energy penetrators—the 'Bulging Effect' analysis. Materials (Basel) 2021;14(12):3334.